Numerical Filtering of Spurious Transients in a Satellite Scanning Radiometer: Application to CERES

G. LOUIS SMITH

Virginia Polytechnic Institute and State University, and NASA Langley Research Center, Hampton, Virginia

D. K. PANDEY

Science Applications International Corp., Hampton, Virginia

ROBERT B. LEE III, BRUCE R. BARKSTROM, AND KORY J. PRIESTLEY

Atmospheric Sciences Division, NASA Langley Research Center, Hampton, Virginia

(Manuscript received 5 January 2001, in final form 16 July 2001)

ABSTRACT

The Clouds and Earth Radiant Energy System (CERES) scanning radiometer was designed to provide high accuracy measurements of the radiances from the earth. Calibration testing of the instruments showed the presence of an undesired slow transient in the measurements of all channels at 1% to 2% of the signal. Analysis of the data showed that the transient consists of a single linear mode. The characteristic time of this mode is 0.3 to 0.4 s and is much greater than that the 8–10-ms response time of the detector, so that it is well separated from the detector response. A numerical filter was designed for the removal of this transient from the measurements. Results show no trace remaining of the transient after application of the numerical filter. The characterization of the slow mode on the basis of ground calibration data is discussed and flight results are shown for the CERES instruments aboard the Tropical Rainfall Measurement Mission and *Terra* spacecraft. The primary influence of the slow mode is in the calibration of the instrument and the in-flight validation of the calibration. This method may be applicable to other radiometers that are striving for high accuracy and encounter a slow spurious mode, regardless of the underlying physics.

1. Introduction

The Clouds and Earth Radiant Energy System (CERES) scanning radiometer (Barkstrom 1990; Wielicki et al. 1997) was designed to provide high accuracy measurements of the radiances from the earth in three wavelength bands: total (0.2–100 μm), shortwave (0.2–5.0 μm), and the longwave window channel (8–12 μm). From these broadband radiance measurements, the radiative fluxes leaving the ''top of the atmosphere'' can be computed. CERES instruments flew aboard the Tropical Rainfall Measurement Mission (TRMM) and the *Terra* spacecraft and are to fly aboard the Aqua spacecraft. The TRMM was placed into orbit in November 1997. Its orbit covers 35°N–35°S and precesses through all local times every 48 days. In addition to a CERES instrument, the TRMM spacecraft includes a precipitation radar, a microwave imager, a Visible and Infrared Scanner and a Lightning Sensor. The PR permits computation of latent energy release within clouds as a concomitant to the radiant flux at the top of the atmosphere in order to help understand the energetics of the Tropics. The *Terra* spacecraft was launched into a sun-synchronous orbit crossing the equator at 1030 LT in December 1999. *Terra* includes the Moderate Resolution Imaging Spectroradiometer (MODIS), which provides cloud data to help diagnose cloud properties to aid in understanding the CERES radiances. The Aqua spacecraft will also carry a MODIS and infrared and microwave sounders for retrieving atmospheric temperature and humidity profiles. Its orbit will be sun synchronous, crossing the equator in midafternoon.

The CERES instruments are calibrated in vacuum to better than 1% accuracy and precision approaching 0.3% (Lee et al. 1996, 1998, 1999, 2000; Barkstrom et al. 2000; Smith et al. 2000). As a consequence, it is possible to detect small imperfections in the dynamic responses of these instruments. Calibration testing of the proto-flight model (PFM) of the instrument, which flew on the TRMM spacecraft, showed the presence of an undesired slow transient in the measurements from all three channels. This transient is about 1%–2% of the

Corresponding author address: Dr. G. Louis Smith, NASA Langley Research Center, Mail Stop 420, Hampton, VA 23681-2199.
E-mail: g.l.smith@larc.hasa.gov

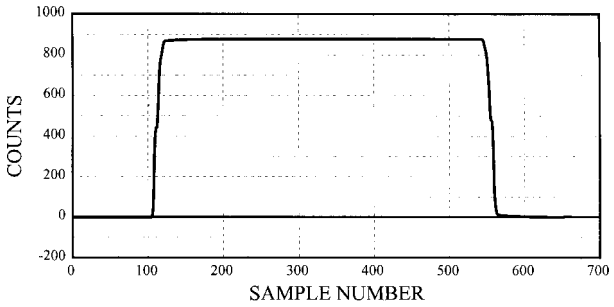

FIG. 1. Response of the total channel of the PFM as function of sample number as it views internal blackbody.

true signal, depending on the channel, and damps out over a characteristic time of 0.3–0.4 s. At the time the transient was found, it would have been prohibitively expensive to modify the hardware to eliminate the transient, and there is no guarantee that such an effort would have succeeded.

One of the major effects of the transient is that it corrupts the measurement when the instrument scans to stare at space for a zero radiance value (the ''space look''), causing an offset in all measurements during the preceding and succeeding scans. Another major effect is that during in-flight calibration the measurement does not approach its asymptotic value during the time available, thereby creating errors in the computed gain of the channel if not taken into account. Also, as the instrument scans from the space look across the earth, the transient causes the measurement to be low as it scans onto the limb. Finally, as the instrument scans from a cold bright cloud to a warm dark surface, the transient will cause a loss in sharpness of the change.

In this paper we discuss a numerical filter for the removal of this transient from the measurements. In order to remove this spurious signal, it is necessary to characterize its behavior, which is defined by two constants. A method for deriving these constants from the data is developed. Finally, results of application of this numerical filter to the CERES instrument aboard the TRMM and *Terra* spacecraft data are shown. No trace of the transient is discernible after application of the numerical filter. For the in-flight calibration results quoted by Lee et al. (1998, 2000), the numerical filter was used.

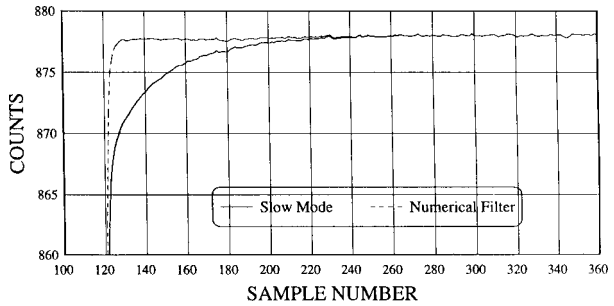

FIG. 2. Asymptotic portion of response of total channel of PFM as function of sample number as it views internal blackbody.

The slow response was found because the calibration permitted accuracies of a fraction of a percent. At this level, one expects many problems to occur. The present technique may be applicable to other instruments which encounter response transients in operation.

2. Background

The CERES instruments each have three channels: a total channel (0.2–50+ μm), a shortwave channel (0.2–5.0 μm), and a window channel (8–12 μm). These instruments were calibrated in the Radiometric Calibration Facility (Lee et al. 1996). Figure 1 shows a time history of the output of the total channel of the PFM as the instrument scans onto and stares at the wide field-of-view blackbody in the Radiometric Calibration Facility. The output rises very quickly to about 98% of its peak value, then has a slow transient in its approach to its asymptotic value, shown in Fig. 2. The design response time of the instrument—that is, the primary thermal mode of the detector—is on the order of 10 ms, which is the data-sampling rate. This mode is shown by the initial rapid rise. The slow transient that follows can be characterized as a slow mode with a characteristic time on the order of 300–400 ms and an amplitude of 1%–2% of the signal. Similar results were found for the longwave window channel (8–12 μm) and the shortwave channel (0.2–5.0 μm). In order to treat the slow mode, it is first useful to examine the mechanism of the slow mode and to consider the various time scales of importance to the CERES instrument.

a. Mechanism of slow mode

Each channel of the CERES instrument consists of a Cassegrain telescope, which focuses radiation from the scene onto a thermistor bolometer (Fig. 3). This active thermistor bolometer is mounted on a heat-sink disk. The active thermistor bolometer is connected with a bridge circuit to a compensator thermistor bolometer, which is mounted on the back side of a second heat-sink disk in an enclosure in order to maintain constant radiation and temperature. The active and compensator thermistor bolometers are selected from those available to be as nearly identical as possible. The two disks are bolted together with an indium gasket between them to increase thermal conductivity. A titanium gasket reduces thermal conduction from the heat-sink disks to the field stop. In essence, the measurement is proportional to the difference of temperature between the active and compensator thermistor bolometers. The temperature of the disk subassembly is maintained as nearly as possible at a constant level by an electric feedback loop, which has a time response of several minutes.

The slow mode has been simulated quite closely by a highly detailed numerical model (Priestley 1997;

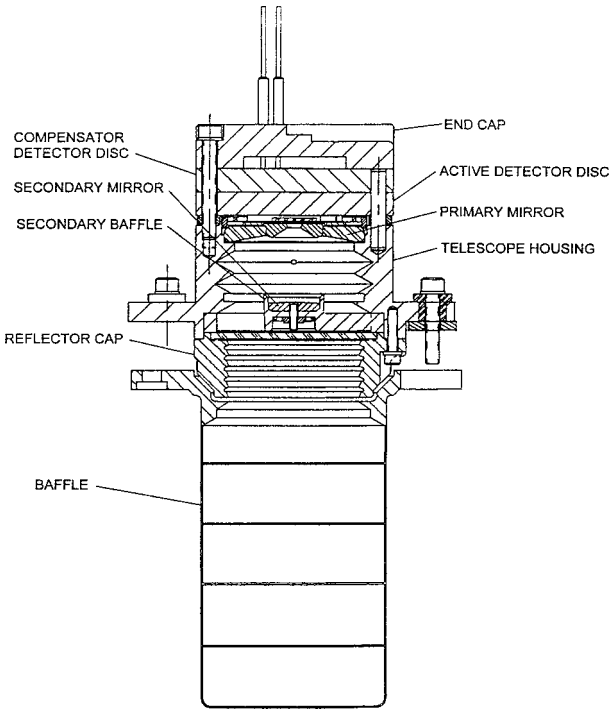

FIG. 3. Design of radiometer.

Haeffelin et al. 1997). The spurious mode is due to heating of the heat-sink disk to which the active thermistor bolometer is attached, as indicated in Fig. 4. When radiation from the scene is focused onto the active thermistor bolometer, it heats up with a characteristic time of 8–10 ms to provide the measurement. As the radiation continues, the heat-sink disk to which the active thermistor bolometer is attached heats up, permitting the active thermistor bolometer temperature to rise and increase the temperature difference between it and the compensator thermistor bolometer and increasing the measurement. The characteristic time for this mode of heating is 0.3–0.4 s.

b. Timescales

The timescales relevant to the CERES scanning radiometer are shown in Fig. 5. The output is sampled every 10 ms. Any time response of the radiometer faster than 10 ms cannot be resolved from the data and must

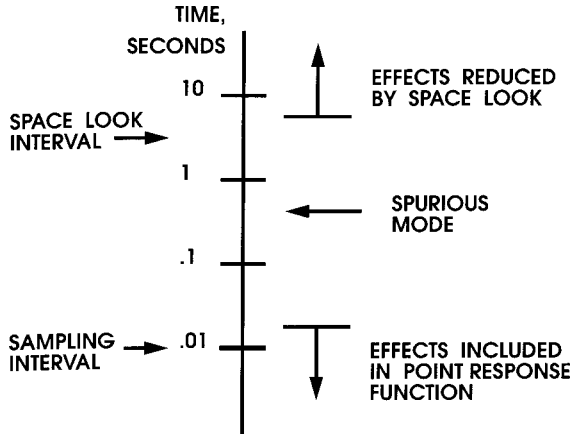

FIG. 5. Characteristic times of radiometer.

be included in the point response function. The radiometer looks at space every 3 s in order to get a zero radiance reading. The zero radiance reading is linearly interpolated between space looks. Over a period of several minutes the zero radiance value may drift significantly. Also, the temperature-stabilization feedback loop for the disk subassembly acts over a period of several minutes. Any time response longer than the time between space looks will be attenuated by the subtraction of the zero radiance readings from the measurements. Between the data-sample period and the space look period is a 2 1/2 order of magnitude span within which one hopes there are no detectable time responses. However, in the CERES scanning radiometer this spurious mode appears with a 0.3–0.4-s time response at the 2% level. This mode is sufficiently slow that its effects can be uncoupled from the point response function and resolved by the data, so that it is possible to remove any significant effects by a numerical filter.

3. Numerical filter formulation

a. Formulation of slow mode response

Figure 6 shows the basic concept upon which the numerical filter is based. As the result of an input radiance $r(t)$, a signal $u(t)$ is generated. The signal can be expressed in terms of an integral over the field-of-view of the scene radiance weighted by the point response function. The angular distance in the scan direction is

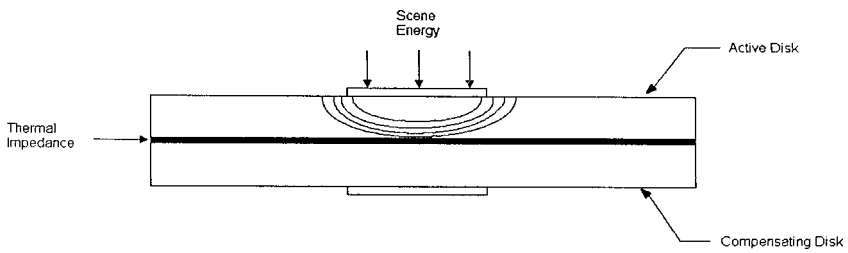

FIG. 4. Mechanism causing slow mode.

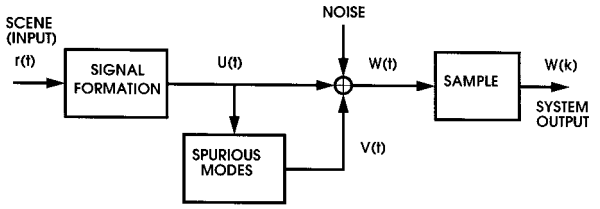

FIG. 6. Block diagram of radiometer response.

mapped into time t and the variation of the scene in the direction normal to the scan is ignored in the present treatment, reducing the problem to one dimension. Thus, the signal is

$$u(t) = \int_{\text{FOV}} P(t' - t)r(t')\,dt'. \tag{1}$$

The data rate, instrument field-of-view (FOV) and the signal conditioner (a four-pole Bessel filter) have been matched to the time response of the detector so as to minimize alias and blur errors in the retrieved field (Manalo and Smith 1991; Manalo et al. 1991).

A basic principle of design is that the signal formation should not pass significant power at frequencies higher than the Nyquist frequency. All frequency components in the scene $r(t)$ faster than the Nyquist frequency are attenuated from $u(t)$ by the sensor design, which includes selection of the field-of-view size and shape, the detector response time and the Bessel filter. These high frequency components are a major distinction between $u(t)$ and $r(t)$. The second major distinction is that the spectral components of $u(t)$ with frequencies near the Nyquist frequency are reduced in amplitude, which is blur, and usually delayed in phase, which is distortion. The phase delay is accounted for by locating the data at the centroid of the point response function.

Unfortunately, due to heating of the heat sink of the active thermistor–bolometer, one or more spurious modes are superimposed on the signal. The response of the spurious modes as they appear in the output is denoted as $v(t)$. The measurement $w(t)$ is thus given by the detector output with the spurious modes superimposed:

$$w(t) = u(t) + v(t). \tag{2}$$

In order to achieve the desired accuracy from the measurements $w(t)$, it is necessary to remove the spurious mode $v(t)$. We wish to retrieve the undistorted signal $u(t)$, for which the design is already optimized on the basis of alias and blur errors, and not $r(t)$.

The spurious modes are assumed to be driven by heat going into the sensor, which is proportional to the undistorted signal $u(t)$, so that (see appendix)

$$g\left(\frac{d}{dt}\right)v(t) = h\left(\frac{d}{dt}\right)u(t). \tag{3}$$

Because conduction is a linear process, $g(d/dt)$ and $h(d/dt)$ are linear operators consisting of polynomials in the time derivative. The degree of the g polynomial is the number of significant modes which contribute to the transient response and the degree of h is one less. Equations (2) and (3) can be combined to give the spurious transient due to the slow modes in terms of the measurement:

$$\left[g\left(\frac{d}{dt}\right) + h\left(\frac{d}{dt}\right)\right]v = h\left(\frac{d}{dt}\right)w. \tag{4}$$

Although the present problem is due to transient heat flux between the active and compensating thermistor bolometers, Eq. (3) does not depend on the details of the underlying physics, but only states that the process is governed by a linear differential equation. Also, the equation has constant coefficients, which simplifies the present application so that the numerical filter likewise has constant coefficients. A system with time-varying coefficients could be treated in a similar manner.

At this point a number of modes could be included; the a priori assumption is made that only one mode is needed to describe the spurious transient of the CERES scanning radiometer. The justification (or rejection) of this assumption will depend on the results. Thus the operator on the left hand side of Eq. (3) reduces to first order:

$$g\left(\frac{d}{dt}\right) = \frac{d}{dt} + \lambda, \tag{5}$$

where λ is the inverse of the characteristic time of the mode. The operator on the right-hand side is then of 0th order and reduces to $c\lambda$, where c is the loading of the slow mode into the signal. For a single mode spurious response, Eq. (4) reduces to

$$\frac{dv}{dt} + \lambda(1 + c)v = c\lambda w. \tag{6}$$

The solution of Eq. (6) can be expressed in terms of the measurements $w(t)$ as

$$v(t) = c\lambda \int_{-\infty}^{t} I(t - t')w(t')\,dt', \tag{7}$$

where $I(t)$ is the impulse response function for the operator $(g + c\lambda)$. In particular, for the single-mode case,

$$v(t) = c\lambda \int_{-\infty}^{t} \exp[-\lambda(1 + c)(t - t')]w(t')\,dt'. \tag{8}$$

Equation (8) gives the effect of the spurious mode on the measurement in terms of the measurement history.

b. Derivation of numerical filter

The measurement $w(t')$ is known only at discrete points t_j. Because the spurious mode is slow, $w(t')$ can

be approximated as piecewise constants based on $w(t_j)$. Equation (8) may thus be written as

$$v(k) = p_1 \sum_{j=k}^{-\infty} p_0^{k-j} w(j), \tag{9}$$

where

$$p_0 = \exp[-\lambda \Delta t(1 + c)],$$
$$p_1 = c(1 - p_0)/(1 + c). \tag{10}$$

Equation (9) is a very inefficient form for application. This solution can be generated recursively by writing Eq. (9) for $v(k - 1)$, whence it is seen that

$$\tilde{v}(k) = p_0 \tilde{v}(k - 1) + p_1 w(k). \tag{11}$$

The tilde is used to denote that this is a computed estimate of the quantity. Equation (11) can also be derived as the solution of the difference equation which corresponds to the differential equation (6) in finite form. Equation (11) permits the efficient computation of the spurious mode recursively during data processing. Once the $\overline{v}(k)$ is computed, the retrieved measurement can be computed as

$$\overline{u}(k) = w(k) - \overline{v}(k). \tag{12}$$

c. Application of numerical filter

The modal loading factor c and the modal time constant λ^{-1} are different for each detector due to manufacturing differences. Once these constants are determined from calibration data, the p_0 and p_1 are computed. For each measurement $w(k)$, the spurious mode amplitude $\overline{v}(k)$ is computed using Eq. (11) and the retrieved measurement $\overline{u}(k)$ is computed by use of Eq. (12). The algorithm requires only the storage of the immediately preceding transient amplitude $v(k - 1)$.

In order to start the filter at the very beginning or after a disruption of data flow, the transient mode is assumed to be in equilibrium with $w(k)$ for expediency, so that we let

$$\overline{v}(k - 1) = w(k) \frac{c}{(1 + c)},$$

for the initial conditions only. Equations (11) and (12) are then used for processing the data. After a few characteristic times λ^{-1}, the effect of the initial condition will be damped out exponentially. Standard procedure is to begin count conversion to raw radiances with the scanning of space. During this time, the initial condition will damp out.

d. Response of measurement to step input

The response of the measurement to a step radiance input is now considered. The response of the undistorted output $u(t)$ as the radiometer scans onto a unit step input is denoted as $F(t)$, where $F(t) \to 1$ for large t. The spurious mode is then given from the solution of Eqs. (3) and (4) as

$$v(t) = Gc\lambda \int_{-\infty}^{t} \exp[-\lambda(t - t')] F(t')\, dt'. \tag{13}$$

Even though $F(t)$ is a smooth function at the timescale of the pixel response during calibration, at the timescale of the slow mode it can be considered to be a step function. In order to reduce errors due to this approximation, the step is assumed to occur at the centroid of the pixel, which we denote as t_1. For $t > t_1$, $F(t) \approx 1$ and $v(t)$ can be written as

$$v(t) = Gc[1 - e^{-\lambda(t - t_1)}]. \tag{14}$$

The measurement is then

$$w(t) = G + Gc[1 - e^{-\lambda(t - t_1)}], \tag{15}$$

and the asymptotic value of the measurement is

$$w_{asy} = G(1 + c). \tag{16}$$

Equation (16) shows that the slow mode does not vanish at large t, but takes a steady-state value.

The slow mode affects the gain computation of the instrument. In the absence of the slow mode, the instrument counts for a unit input would be $q = G$. During ground calibration, the total and longwave window channels stare at the blackbody for more than 3 min. During this time, the slow mode does not vanish, but approaches a nonzero steady state Gc. Equation (16) shows that the instrument counts are $q = G(1 + c)$. The apparent gain G' is computed on the basis of this steady state, thus is $G' = q/(1 + c)$ and includes the steady-state value of the slow mode. This apparent gain G' is reduced from the true gain G:

$$G' = G/(1 + c). \tag{17}$$

In order to use the apparent gain, that is, the result from the steady state, the factor $(1 + c)$ is included in Eq. (12):

$$\overline{u}(k) = [w(k) - \overline{v}(k)](1 + c). \tag{18}$$

For the CERES computations, Eqs. (11) and (18) should be applied to filtered radiances, after accounting for the offsets and space clamp. This is most easily done by incorporating the factor $(1 + c)$ in the p_0 and p_1. By writing the equations in this manner, the numerical filter results match the results obtained from the steady-state calibrations. One advantage of this procedure is that the steady state results using the numerical filter are independent of the modal amplitude c. In the data processing, after the instrument counts are converted to radiances, the numerical filter is used to retrieve the undistorted radiance.

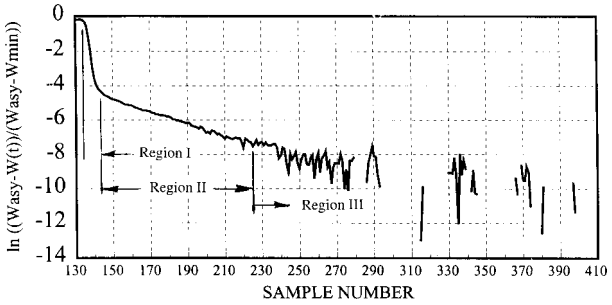

FIG. 7. $\ln[(w_{asy} - w(t))/(w_{asy} - w_{min})]$ as function of time as total channel scans to view internal blackbody.

4. Determination of slow mode characteristics from ground calibration data

In order to apply the numerical filter to eliminate the transient mode from the data, it is necessary to determine the two parameters λ and c, which govern the dynamic response of the slow mode, from the ground calibration data. In ground calibration testing the slow mode is most evident when the total or longwave window channel scans from the cold reference (Lee et al. 1996) to stare at the wide-field-of-view (WFOV) blackbody for a period of more than 3 s. Similar data are also taken when these channels stare at the internal blackbodies for the purpose of calibrating the internal blackbodies. Scanning of the total channel from the cold reference to stare at the WFOV blackbody or the internal blackbody approximates a step input to the sensor. From Eq. (16) the step response of the system can be expressed in terms of counts as

$$w(t) = w_{asy} - (w_{asy} - w_{min})\left(\frac{c}{1 + c}\right)e^{-\lambda(t-t_0)}. \quad (19)$$

From this form we can write

$$-\lambda(t - t_0) = \ln\left[\frac{w_{asy} - w(t)}{w_{asy} - w_{min}}\right] - \ln(c) + \ln(1 + c). \quad (20)$$

A plot of $\ln[(w_{asy} - w(t))/(w_{asy} - w_{min})]$ will thus have a slope of $-\lambda$ when the basic time response of the detector has damped out, leaving only the slow mode response. Figure 7 shows $\ln[(w_{asy} - w(t))/(w_{asy} - w_{min})]$ as a function of time for the total channel of the CERES PFM as it views the internal blackbody during ground calibration testing. The plot shows three regions of response. In region I the instrument is scanning onto the calibration source and the detector and signal conditioning circuitry are coming into equilibrium. Because the input is not a perfect step function the instrument response is quite complicated in this region. In region II the response is linear, indicating that the only variation is due to the slow mode and Eq. (20) applies. The slope of the response in this region is $-\lambda$, the inverse of the characteristic time. In region III the slow mode is small enough that the noise begins to mask the slow mode behavior. Positive noise on the measurement causes $w(t)$ to exceed w_{asy} so that the logarithm becomes imaginary, resulting in gaps in the plot.

The linearity of the response curve in region II is fundamental to the present technique, because it shows that there is only one spurious mode of concern with characteristic time in this range, as a second mode would cause extra terms which would create curvature. A slower mode would be of importance at larger times, which being in region III must be smaller than the noise level. A faster mode would appear at smaller times, that is, in region I. Such a mode would have appeared in testing of the point response function (Paden et al. 1997) if it were present.

In order to plot Fig. 7, a value of w_{asy} is required. The initial estimate comes from inspection of Fig. 2. If the value used for w_{asy} is too large, the curve of Fig. 7 will approach a constant value. If the value is too small, the curve will turn sharply down. By noting the behavior of $\ln[(w_{asy} - w(t))/w_{asy} - w_{min})]$ as a function of time, one can iterate on the value of w_{asy} to get its value quite accurately. Sufficient accuracy is achieved when the response is straight in region II and the initial part of region III.

We now consider the computation of the modal loading c. If the input to the slow mode were a step function, then from Eq. (19);

$$\frac{c}{1 + c} = \frac{w_{asy} - w_0}{w_{asy} - w_{min}}, \quad (21)$$

where w_0 is the measurement after the rapid response of the undistorted signal, that is, the primary mode of the detector, has damped out. The input to the slow mode is not a step response, but is the response of the detector to the source as the instrument scans onto the source, which constitutes region I. Because the primary mode of the detector is fast compared to the slow mode, that is, these two modes are well separated, region I is of short duration compared to region II. We select the midpoint of region I as the time at which a step input is applied. The straight line of region II is then extrapolated to this t_0 to give w_0, so that the right-hand side of Eq. (21) and c can be computed. Fortunately, the slope of the line, $-\lambda$, is small so that c is not sensitive to the estimate of t_0.

The numerical filter was applied to the PFM total channel calibration data and the results are shown in Fig. 2 as a dotted line using $c = 0.026$ and $\lambda = 9.45$. The measurements approach the asymptotic value with a characteristic time of 9 ms, corresponding to the response time of the detector. The slow mode does not appear, indicating that the numerical filter does work and the parameters selected are suitable.

5. Flight results of numerical filter for PFM

The numerical filter was applied in the data processing for the CERES PFM instrument aboard the *TRMM*

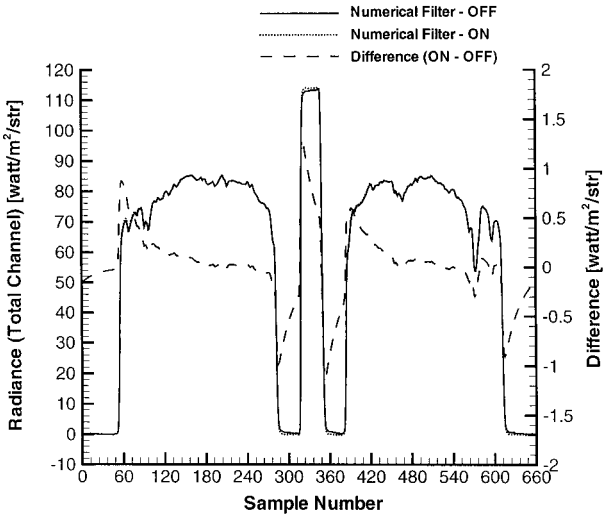

FIG. 8. Average total channel radiances for 1 h as a function of sample number for PFM in flight.

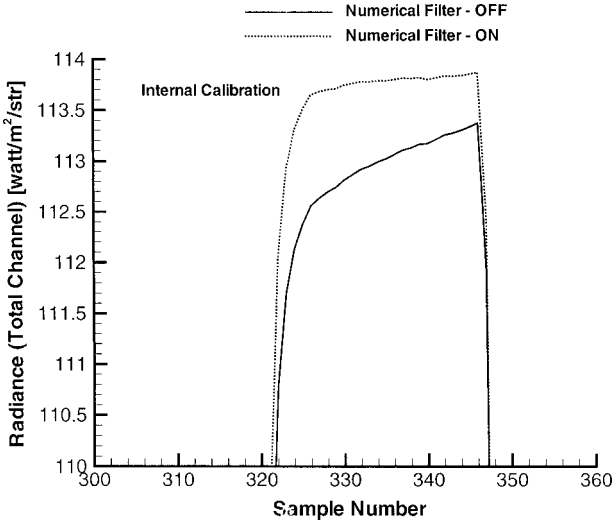

FIG. 9. Average total channel response for 1 h as it scans onto internal blackbody in flight.

spacecraft and to the flight models 1 and 2 (FM-1 and -2) aboard the *Terra* spacecraft. The CERES instrument scans from the space look at 8° (horizontal is taken as zero) across the earth to another space look at 162° and then to 194° (i.e., 14° above horizontal), where it stops for a short time to view the Internal Calibration Module (Smith et al. 1998). The measurements from the PFM total channel for a scan on 5 August 1998 are shown as a function of sample number in Fig. 8. The radiances computed without the numerical filter are shown as a solid line and with the numerical filter by a dotted line. The same gains are used for both cases. The difference between the radiances with and without the numerical filter is also shown as a dashed line with the enlarged scale on the right axis. Each scan takes 6.6 s and a measurement is taken once every 10 ms so that at sample number 660 the scan cycle repeats. The scan begins with the space look at 8° scan angle to establish zero radiance. At approximately sample 60 the instrument begins to scan across the earth. At approximately sample 290 the instrument scans from earth to space (near scan angle 162°) and at sample 310 scans to look at the Internal Calibration Module (ICM), where the total channel views the Internal Blackbody. At sample 350 the instrument scans from the ICM to space (again near scan angle 162°) and at sample 380 has scanned onto the Earth for another scan, until sample number 610, where the instrument has returned to the starting position. The effects of the numerical filter are seen in regions where there is a large change, that is, as the instrument scans onto the limb of the earth, as it scan onto the internal blackbody and as it scans to the space look. The rest of the time, the effect of the numerical filter is very small in the average.

Figure 9 shows the approach of the total channel measurements to equilibrium while looking at the internal blackbody. Without the numerical filter (solid line) the measurement does not reach steady state during the time available for the internal calibration and causes the measurement to be 0.5 W m^{-2} sr^{-1} less than the asymptote at the end of the internal calibration period. The retrieved undistorted measurements, that is, with the numerical filter (dotted line), quickly come within 0.1 W m^{-2} sr^{-1} of its asymptote, with the 9-ms response time of the detector apparent. If not accounted for, this difference together with the difference at the space look would cause an error in the inflight calibration results for the gain of the channel. This error of gain would then affect all measurements.

The output of the detector is given by the number of counts above the zero radiance level, which is converted to radiance units by multiplying by the gain of the channel. The zero level drifts over a period of several minutes and is established for each scan by the space look. Figure 10 shows the space look measurements in detail. As the instrument scans from viewing earth to space at scan angle 8°, the slow mode is obvious in the measurements without the numerical filter applied (solid line). The zero radiance value is taken to be the average of the measurements from 13 samples, typically sample number 28 to 40. During the space look it is possible to get small negative values of radiance due to random errors below this average value. With the numerical filter applied, the retrieved measurements very quickly drop as expected for the 9-ms first-order response of the detector and remain steady over the period of the space look. Any error in the space look causes an error in each measurement of earth radiances. No trace of the desirable transient is discernible in the retrieved measurements; only residual noise at the 0.02 W m^{-2} sr^{-1} level remains. The space look is especially valuable for validating the numerical filter because it demonstrates that the transient mode is due to effects within the scanner

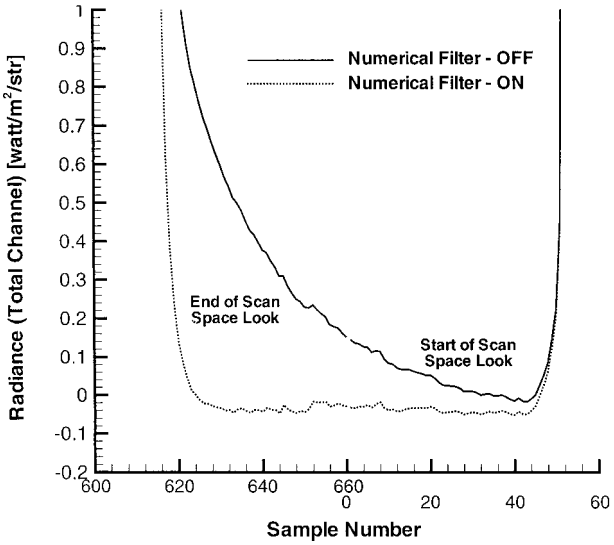

FIG. 10. Average total channel counts for space look for 1 h as a function of sample number for PFM.

alone and is not due to a mode which may be conjectured as created by a radiative coupling between the telescopes and the internal calibration sources when data from these devices are used. Also, the flatness of the retrieved measurements during the space look provides validation of the assumption of a single linear mode to describe the spurious transient.

The radiances from the total channel of the PFM during the space looks just prior to and after the internal calibration are shown in Fig. 11. These space looks are not usually used in data processing, but are for validating that this space look is compatible with those at scan angle 8°. Without the numerical filter, the radiance

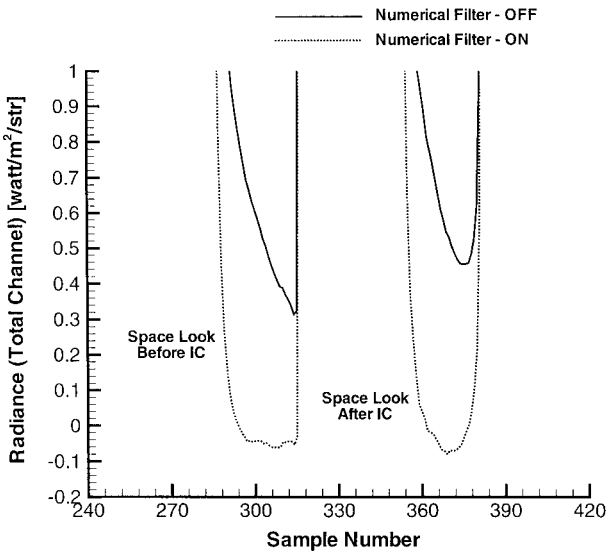

FIG. 11. Average total channel response for 1 h for space look on internal calibration module side of scan for PFM.

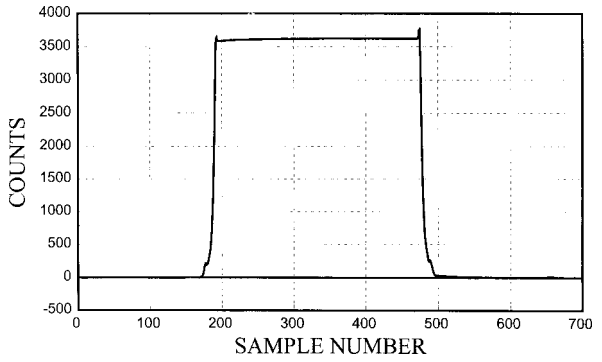

FIG. 12. Shortwave channel response to the SWICS for FM-1.

measurements do not reach the steady state value. By applying the numerical filter, the retrieved radiances indicate the zero radiance level to be -0.06 W m^{-2} sr^{-1}, which would be a much smaller error than the 0.3 W m^{-2} sr^{-1} indicated by the raw measurement. There are cases in which the space look is contaminated or lost in the data stream for various reasons. In such cases, the space look near scan angle 162° can be used after application of the numerical filter.

The application of the numerical filter to the CERES Flight Models 1 and 2 aboard the *Terra* spacecraft is now described. Figure 12 shows the shortwave channel response to the Shortwave Internal Calibration Source (SWICS) for FM-1. There is a small overshoot of the response above the aymptotic value as the detector scans onto the SWICS and again as it scans away from the SWICS, due to extraneous reflections at the edge of the SWICS. Figure 13 shows $\ln[(w_{asy} - w(t))/(w_{asy} - w_0)]$ for these measurements. The response overshoot results in the dip at sample number 192, after which the curve shows the linear behavior of the slow mode. The overshoot was so quick that the slow mode does not significantly respond. From the slope of the curve, λ is computed to be 2.9 s^{-1} and extrapolation of the line back to the initiation of the SWICS input gives $c = 0.016$.

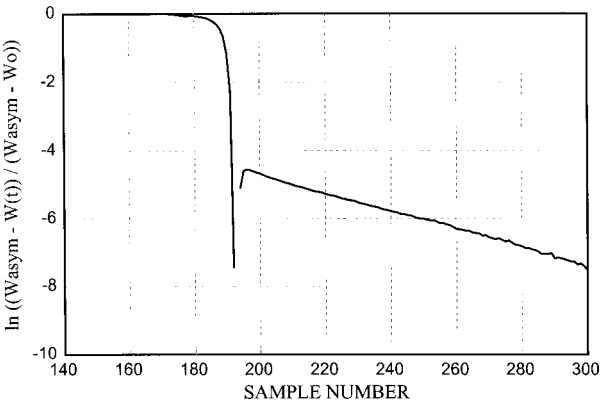

FIG. 13. $\ln[(w_{asy} - w(t))/(w_{asy} - w_{min})]$ as a function of sample number for FM-1 shortwave channel as it views the SWICS.

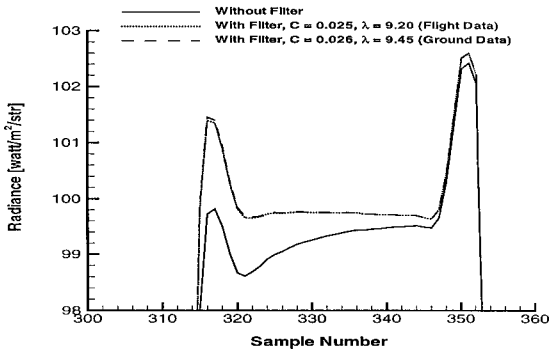

FIG. 14. Total channel response to internal blackbody for FM-2 instrument with and without numerical filter.

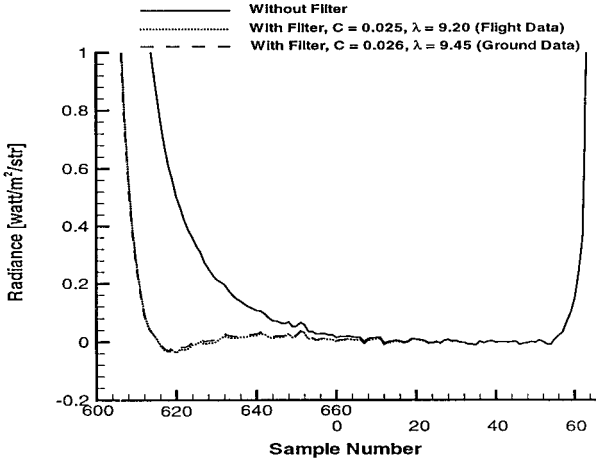

FIG. 15. Total channel response during space look for FM-2 instrument with and without numerical filter.

Figure 14 shows the effect of applying the numerical filter to the total channel data from the FM-2 instrument during the use of the internal blackbody (IBB) for in-flight calibration checks. The solid line is the response of the detector without accounting for the slow mode. The dashed line shows the response with the slow mode taken into account using the parameters determined from ground calibration data and the best fit parameters from in-orbit data are used for the dotted line. As the total channel scans to look at the IBB, it sees shortwave and longwave radiation scattered and emitted from the interior of the instrument, which causes the overshoot peak of 1.6 W m^{-2} sr^{-1}. After the detector stops at the IBB position, the slow mode continues to vary throughout the duration of the IBB measurement. Between sample numbers 320 and 343 the radiance value with the slow mode numerically filtered out varies less than 0.1 W m^{-2} sr^{-1}. The parameters determined from ground calibration data and from flight data give results that are nearly indistinguishable. For this channel the effect of the numerical filter is to change the radiance by 1.2 W m^{-2} sr^{-1} at the beginning of the internal calibration period.

Figure 15 shows the effects of the numerical filter on the space look radiance values for the total channel. The sample numbers start with zero at the center of the space look, after which the detectors scan the earth, take a short space look on the other side, and then look at the calibration devices, scan back across the earth to the initial space look and repeat (Smith et al. 1998). The abscissa begins with the scanning of the detectors to space and continues across the zero sample number position at which point a new data frame begins. The radiance for each position is the mean for that sample number for scans taken over a 1/2-h period. With the numerical filter, the radiance level is 0.04 W m^{-2} sr^{-1} by sample number 615, but without the numerical filter the radiance level does not drop to 0.04 until sample number 652. Application of the numerical filter considerably increases the length of time available for the determination of the zero radiance level. This is especially important during times when artifacts or data disruptions occur in the space look. One such case is when the moon appears in the space look.

The shortwave channel response for the space look is shown by Fig. 16 for FM-2. The values of the parameters computed from ground calibration ($c = 0.023$, $\lambda = 8.2$) result in an undershoot of the radiance but parameters ($c = 0.013$, $\lambda = 8.6$) computed using flight data and a best mean square fit procedure give radiance values which are within 0.1 W m^{-2} sr^{-1} of 0 for sample number 612. The flight parameters will be incorporated into the data processing for the FM-2 shortwave channel. Additional information about the FM-1 and -2 slow mode characterizations, including the description of the best mean-square fit method is given by Smith et al. (2000).

6. Discussion

As the instrument scans from the space look to the earth, the effect of the slow mode is to cause the mea-

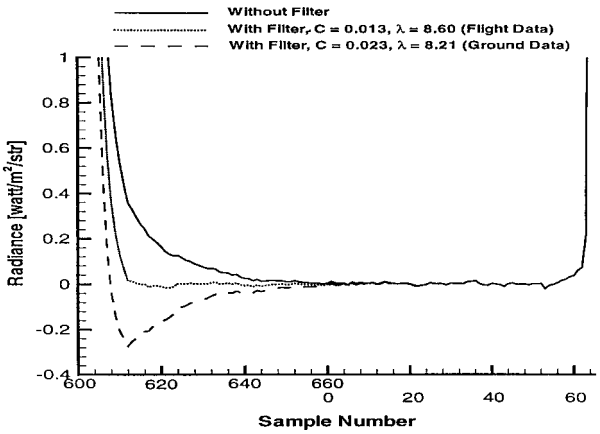

FIG. 16. Shortwave channel response for space look for FM-2 instrument with and without numerical filter.

surements to be low until the instrument has scanned through 40° of nadir scan angle, by which time the effect of the slow mode has decreased. The numerical filter eliminates this effect. When the instrument scans from one scene to another with greatly differing radiances, for example, from tropical land to the top of a deep convective cloud, the instrument indicates an OLR radiance which is high initially by approximately 2% of the change, due to the slow mode. As the instrument scans from the cold cloud top to warm land, the lag causes the instrument to indicate a radiance which is low initially. These differences average out and do not appear in averages over large areas that are well away from the limb. For this reason, the major effect of the numerical filter is in establishing the correct zero radiance value during the space look and the correct results from the internal calibration data. These values affect all measurements.

The fact that the spurious signal is small and its time response is well separated from the rest of the system response modes simplified the implementation of the numerical filter, but is not a requirement in the design of the numerical filter. Likewise, if additional modes were present in the instrument output, they would complicate the development a numerical filter, but would not prevent it.

Further resolution enhancement of the image is not attempted with this numerical filter, as the CERES instrument was designed to minimize the sum of blur and alias errors near nadir. It may be possible to design a numerical filter that would enhance resolution in the along-track direction away from nadir, where the overlapping of pixels increases greatly, but that is beyond the intent of this paper.

7. Conclusions

During calibration testing of the CERES proto-flight model, a spurious slow response was found with a characteristic time of 0.3–0.4 s, an order of magnitude slower than the primary time response mode. A numerical filter is developed here for removal of this spurious response. This method does not depend on the details of the underlying physics of the transient, but only requires that the response be linear. It is demonstrated that the slow response is due to a single mode. Ground calibration data are used to compute the modal response time and amplitude for the spurious mode. Application to flight data for the proto-flight model and for flight models 1 and 2 aboard the *Terra* spacecraft shows that the numerical filter eliminates the slow mode from the measurements; only residual noise from other effects remain.

The effects of the slow mode are primarily in the in-flight calibration of the instrument, whereby the slow mode prevents the instrument from attaining a steady state during the time available for the space look, which is required to establish the zero-radiance counts and for the standard in-flight calibration sequence. The numerical filter does not affect averages over large areas away from the limb of the earth onto which the instrument scans from space.

Acknowledgments. This work was supported by the Earth Science Enterprise of NASA through Langley Research Centre by Cooperative Agreement NCC1-405 to Virginia Polytechnic Institute and State University and Contract NAS1-19579 to Science Applications International Corp.

APPENDIX

Relation of Spurious Transients to Undistorted Measurements

The spurious transients in the measurements are due to slow modes of heat transfer within the thermistor bolometer assembly. The relation of these transients to the undistorted measurement is based on the time-dependent temperature distribution within the assembly, which consists of the thermistor bolometer, the paint layer which absorbs the radiation to be detected and which is bonded to the thermistor bolometer, and the active and compensator disks. The equation for the temperature distribution within the detector assembly is

$$c\frac{\partial}{\partial t}T = \nabla \cdot (k\nabla T) + q, \tag{A1}$$

where q is a heat source in the detector. The heat source of primary interest is the radiation that is absorbed in the layer of paint that is bonded to the thermistor bolometer. The method of separation of variables is used, whereby it is assumed that $T(\mathbf{r}, t) = X(\mathbf{r})\phi(t)$, whence

$$-\lambda_n c X_n = \nabla \cdot (k\nabla X_n) + q_n \quad \text{and}$$

$$\frac{d\phi_n}{dt} + \lambda_n \phi_n = f_n(t), \tag{A2}$$

where q_n is the loading of the heating in the n-th mode and $f_n(t)$ is its time variation. The temperature at a point is then

$$T(\mathbf{r}, t) = \sum_{n\in C} X_n(\mathbf{r})\phi_n(t),$$

where C denotes the set of modes which contribute to the temperature. One can include electrical feedback modes in the analysis provided they are linear. Their addition simply adds more equations to the set of Eq. (A2). The measurement of the thermistor bolometer is the integral of the temperature over the region between the electrodes and thus can be written as

$$w(t) = \sum_{n\in C} b_n \phi_n(t). \tag{A3}$$

The complete set of modes C includes the primary response time of the detector, a number of very fast temperature modes to which the thermistor bolometer has

very little response, and also four modes for the response of the Bessel filter. These modes determine the undistorted signal $u(t)$. The set C also includes a set S of slower modes which are spurious and are to be taken into account by the numerical filter. Equation (A3) thus becomes

$$w(t) = u(t) + v(t), \tag{A4}$$

where $v(t)$ is the spurious part of the signal:

$$v(t) = \sum_{n\in S} b_n \phi_n(t). \tag{A5}$$

We now make the approximation, which is fundamental to the application of this method: For the slower modes, the radiative forcing $f_n(t)$ is proportional to the undistorted signal $u(t)$. This approximation relies on the $u(t)$ response being fast relative to each of the slow modes.

The operator $\Pi_{n\in S}(d/dt + \lambda_n)$ is applied to each side of Eq. (A5) and the approximation is used to replace $f_n(t)$ with $u(t)$ times a constant for each n, resulting in

$$\prod_{n\in S}\left(\frac{d}{dt} + \lambda_n\right)v = \sum_{n\in S} c_n \prod_{p\in S(n)}\left(\frac{d}{dt} + \lambda_p\right)u, \tag{A6}$$

and $S(n)$ denotes the set S of spurious modes with the nth mode removed. The c_n is the b_n times the proportionality of response of the nth mode to $u(t)$. The left-hand side of Eq. (A6) is a polynomial in the time derivative operator d/dt, of degree equal to the number of spurious modes which must be taken into account; the right hand side is a polynomial of one degree less. Equation (A6) can be written as

$$g\left(\frac{d}{dt}\right)v(t) = h\left(\frac{d}{dt}\right)u(t). \tag{A7}$$

This equation relates the spurious modes to the undistorted measurements. The solution of Eq. (A7) is

$$v(t) = \sum_{n\in S} e^{-\lambda t}\left[a_n + \int_0^t u(\tau)e^{\lambda\tau}\, d\tau\right].$$

However, $u(t)$ is not observable. Although this equation was derived on the basis of time-dependent heat transfer, the same form of the equation would be found, for example, if the spurious transients were due to time-dependent electronic responses, provided only that the mechanism is linear.

REFERENCES

Barkstrom, B. R., 1990: Earth radiation budget measurements: Pre-ERBE, ERBE, and CERES. *Proceedings of Long-Term Monitoring of the Earth's Radiation Budget,* B. R. Barkstrom, Ed., Vol. 1299, SPIE, 52–60.

——, B. A. Wielicki, G. L. Smith, R. B. Lee, K. J. Priestley, T. P. Charlock, and D. P. Kratz, 2000: Validation of CERES/TERRA data. *Proc. Conf. on Sensors, Systems and Next Generation Satellites VI, EOS/SPIE Symp. on Remote Sensing,* Barcelona, Spain, SPIE, 17–28.

Haeffelin, M. P. A., J. R. Mahan, and K. J. Priestley, 1997: Predicted dynamic electrothermal performance of thermistor bolometer radiometers for earth radiation budget applications. *Appl. Opt.,* **28,** 7129–7142.

Lee, R. B., III, B. R. Barkstrom, G. L. Smith, J. E. Cooper, L. P. Kopia, and R. W. Lawrence, 1996: The Clouds and the Earth's Radiant Energy System (CERES) sensors and preflight calibration plans. *J. Atmos. Oceanic Technol.,* **13,** 300–313.

——, and Coauthors, 1998: Pre-launch calibrations of the Clouds and the Earth's Radiant Energy System (CERES) Tropical Rainfall Measuring Mission and Earth Observing System (EOS) Morning (AM) spacecraft thermistor bolometer sensors. *IEEE Trans. Geosci. Remote Sens.,* **36,** 1173–1185.

——, S. Thomas, B. R. Barkstrom, D. K. Pandey, K. J. Priestley, G. L. Smith, A. Al-Hajjah, and R. S. Wilson, 1999: Analyses of an-orbit determinations of the Clouds and the Earth's Radiant Energy System (CERES) thermistor bolometer sensor zero-radiance offsets. *Proc. SPIE,* **3750,** 482–493.

——, and Coauthors, 2000: Terra Spacecraft CERES flight model 1 and 2 sensor measurement precisions: Ground to flight determinations. *Proc. SPIE,* **4135–05,** 1–12.

Manalo, N. D., and G. L. Smith, 1991: Spatial sampling errors for a satellite-borne scanning radiometer. *Proc. SPIE Symp. on Optical Engineering and Photonics in Aerospace Engineering,* Vol. 1493, Orlando, FL, SPIE, 281–291.

——, ——, and B. R. Barkstrom, 1991: Transfer function considerations for the CERES radiometer. *Proc. Int. Symp. on Image Understanding for Aerospace Applications,* Vol. 1521, Munich, Germany, SPIE, 106–116.

Paden, J., G. L. Smith, R. B. Lee III, D. K. Pandey, and S. Thomas, 1997: Reality check: A point response function (PRF) comparison of theory to measurements for the Clouds and the Earth's Radiant Energy System (CERES) Tropical Rainfall Measuring Mission (TRMM) instrument. *Proc. SPIE,* **3074,** 109–117.

Priestley, K. J., 1997: Use of first principle numerical models to enhance the understanding of the operational analysis of spaceborne Earth radiation budget instruments. Ph.D. dissertation, Virginia Polytechnic Institute and State University, 174 pp.

Smith, G. L., and Coauthors, 1998: Overview of CERES sensors and in-flight performance. *Proc. SPIE Conf. on Opt. Sci. Eng. and Instrum.,* Vol. 3439, San Diego, CA, SPIE, 292–302.

——, and Coauthors, 2000: Determination and validation of slow mode coefficients of the Clouds and the Earth's Radiant Energy System (CERES) scanning thermistor bolometers. *Proc. SPIE on Earth Observing Systems,* Vol. 4135, San Diego, CA, SPIE, 25–38.

Wielicki, B. A., B. R. Barkstrom, E. F. Harrison, R. B. Lee III, G. L. Smith, and J. E. Cooper, 1996: Clouds and the Earth's Radiant Energy System (CERES): An earth observing system experiment. *Bull. Amer. Meteor. Soc.,* **77,** 853–868.